

Gas temperature measurement based on contrast reversal in mid-infrared CO₂ images: supplement

HIDEKI T. MIYAZAKI,*  **TAKESHI KASAYA,**  **MASAHIRO SAITO,**
KAZUYA KIMOTO, YUTARO TSUIKI, AND TETSUYUKI OCHIAI 

National Institute for Materials Science (NIMS), Tsukuba, Ibaraki 305-0047, Japan

*MIYAZAKI.Hideki@nims.go.jp

This supplement published with Optica Publishing Group on 19 May 2026 by The Authors under the terms of the [Creative Commons Attribution 4.0 License](#) in the format provided by the authors and unedited. Further distribution of this work must maintain attribution to the author(s) and the published article's title, journal citation, and DOI.

Supplement DOI: <https://doi.org/10.6084/m9.figshare.32071797>

Parent Article DOI: <https://doi.org/10.1364/OE.596786>

Gas temperature measurement based on contrast reversal in mid-infrared CO₂ images: supplemental document

HIDEKI T. MIYAZAKI,* TAKESHI KASAYA, MASAHIRO SAITO, KAZUYA KIMOTO, YUTARO TSUIKI, AND TETSUYUKI OCHIAI

National Institute for Materials Science (NIMS), Tsukuba, Ibaraki 305-0047, Japan

*MIYAZAKI.Hideki@nims.go.jp

A. Supplementary discussion on the basics of radiative transfer

A.1 Calculation of CO₂ absorption spectrum based on HITRAN

The absorption cross section k_v derived from HITRAN [1] forms the basis of all CO₂ absorption values in this study. By considering all CO₂ isotopologues and assuming the Voigt lineshape, k_v was calculated at various gas temperatures under a pressure of 101,325 Pa. Figure 2(a) in the main text shows k_v for a gas temperature $T_g = 50^\circ\text{C}$, which is used in Fig. 2(c), (d), Fig. 3(a), and (d) (main text). For the calculations in Fig. 3(b) and (c) (main text), k_v spectra at various temperatures were used.

A.2 Quantification of responsivity spectrum of CO₂ imaging camera

The responsivity spectrum R_v (Fig. 2(b), main text) of the CO₂ imaging camera used in this study was measured using the step-scan function of a Fourier transform infrared spectrometer (FTIR). An optical system was mounted at the specimen stage for extracting a collimated light beam from the FTIR, and the infrared light modulated by the interferometer was irradiated across the entire image sensor. The temporal waveform (interferogram) of the average brightness was Fourier-transformed, and the quantitative responsivity spectrum was determined by comparison with the results of a calibrated detector, with a resolution of 2 cm^{-1} , placed at the same position.

A.3 Details of discussion in Sec. 2.3

In this section, we prepare a framework of the radiative transfer equation based on Eq. (5) in the main text, which is applicable to general cases including nonuniform gases as well as uniform ones. To achieve this, it is first necessary to return to the monochromatic radiative transfer equation at frequency (wavenumber) ν (Eq. (3), main text).

In Eq. (3), the gas temperature T_g can be a function of position z . As shown in Eq. (2) of the main text, the optical thickness κ_ν is determined by k_ν , the total volume number density of the gas n , and the concentration (the mole fraction) of the gas c . The concentration c can also be a function of z , and both k_ν and n depend on T_g . Therefore, κ_ν can be influenced by the spatial distribution of T_g as well as that of c .

By defining an effective temperature $T_{\nu g}^{\text{eff}}$ for each frequency ν , the blackbody radiation term $i_{\nu\text{bb}}$ can be separated from the integral over κ_ν^* in Eq. (3):

$$i_\nu(\kappa_\nu) = i_{\nu\text{bb}}(T_s)\exp(-\kappa_\nu) + \int_0^{\kappa_\nu} i_{\nu\text{bb}}(T_g)\exp[-(\kappa_\nu - \kappa_\nu^*)]d\kappa_\nu^*$$

$$\begin{aligned}
&= i_{\text{vbb}}(T_s) \exp(-\kappa_v) + i_{\text{vbb}}(T_{\text{vg}}^{\text{eff}}) \int_0^{\kappa_v} \exp[-(\kappa_v - \kappa_v^*)] d\kappa_v^* \\
&= i_{\text{vbb}}(T_s) \exp(-\kappa_v) + i_{\text{vbb}}(T_{\text{vg}}^{\text{eff}}) [1 - \exp(-\kappa_v)],
\end{aligned} \tag{S1}$$

where T_s is the light source (background) temperature, and

$$i_{\text{vbb}}(T_{\text{vg}}^{\text{eff}}) = \frac{\int_0^{\kappa_v} i_{\text{vbb}}(T_g) \exp[-(\kappa_v - \kappa_v^*)] d\kappa_v^*}{\int_0^{\kappa_v} \exp[-(\kappa_v - \kappa_v^*)] d\kappa_v^*}. \tag{S2}$$

There are two remarks regarding Eqs. (S1) and (S2). First, for a gas with uniform temperature and concentration, $T_{\text{vg}}^{\text{eff}} = T_g$, and Eq. (S1) reduces to Eq. (4) in the main text. Second, $T_{\text{vg}}^{\text{eff}}$ as given in Eq. (S2) corresponds to the contrast reversal temperature T_s^{rev} at frequency ν . This is because, the intensity difference Δi_ν due to the presence of gas, $\Delta i_\nu = i_\nu(\kappa_v) - i_\nu(0) = [i_{\text{vbb}}(T_{\text{vg}}^{\text{eff}}) - i_{\text{vbb}}(T_s)] [1 - \exp(-\kappa_v)] = A_{\text{vg}} [i_{\text{vbb}}(T_{\text{vg}}^{\text{eff}}) - i_{\text{vbb}}(T_s)]$, where A_{vg} is the absorptivity, becomes zero when $T_s = T_{\text{vg}}^{\text{eff}}$; this is the definition of the contrast reversal temperature T_s^{rev} . Detailed results are discussed in the next Sec. B and Fig. S2 for both uniform and nonuniform cases.

Using the relation in Eq. (S1), Eq. (5) in the main text defining the intensity signal $I_R(u)$ (u : column number density) can be written in a more concise form:

$$\begin{aligned}
I_R(u) &= \int_0^\infty R_\nu i_\nu(\kappa_\nu) d\nu = \int_0^\infty R_\nu i_{\text{vbb}}(T_s) \exp(-\kappa_\nu) d\nu + \\
&\int_0^\infty R_\nu i_{\text{vbb}}(T_{\text{vg}}^{\text{eff}}) [1 - \exp(-\kappa_\nu)] d\nu.
\end{aligned} \tag{S3}$$

For the convenience of practical applications, consider a scheme to approximate a nonuniform gas with spatial distribution of temperature and concentration, as a uniform gas with an effective temperature T_g^{eff} and the same column number density u . Equation (S3) can be expressed in terms of two components: blackbody radiation and gas absorption. The blackbody radiation function and the responsivity spectrum (except for its sharp edges) vary slowly with respect to ν , so they can be separated from the gas absorption terms. Then, separated terms are described by experimentally measurable quantities for a uniform gas with an effective temperature T_g^{eff} :

$$\begin{aligned}
I_R(u) &= \int_0^\infty R_\nu i_{\text{vbb}}(T_s) \exp(-\kappa_\nu) d\nu + \int_0^\infty R_\nu i_{\text{vbb}}(T_{\text{vg}}^{\text{eff}}) [1 - \exp(-\kappa_\nu)] d\nu \\
&\approx R_{\nu_0} i_{\text{vbb}}(T_s) \Delta\nu \times \int_{\nu_1}^{\nu_2} \exp(-\kappa_\nu) \frac{d\nu}{\Delta\nu} + R_{\nu_0} i_{\text{vbb}}(T_{\text{vg}}^{\text{eff}}) \Delta\nu \times \int_{\nu_1}^{\nu_2} [1 - \exp(-\kappa_\nu)] \frac{d\nu}{\Delta\nu} \\
&\approx \int_0^\infty R_\nu i_{\text{vbb}}(T_s) d\nu \times \frac{\int_0^\infty R_\nu \exp(-\kappa_\nu(T_g^{\text{eff}}, u)) d\nu}{\int_0^\infty R_\nu d\nu} + \int_0^\infty R_\nu i_{\text{vbb}}(T_g^{\text{eff}}) d\nu \times \\
&\frac{\int_0^\infty R_\nu [1 - \exp(-\kappa_\nu(T_g^{\text{eff}}, u))] d\nu}{\int_0^\infty R_\nu d\nu} \\
&= [1 - A_g(T_g^{\text{eff}}, u)] I_{\text{Rbb}}(T_s) + A_g(T_g^{\text{eff}}, u) I_{\text{Rbb}}(T_g^{\text{eff}}),
\end{aligned}$$

where ν_0 is the center frequency in the bandwidth $\Delta\nu$ ($\Delta\nu = \nu_2 - \nu_1$),

$$I_{\text{Rbb}}(T) = \int_0^\infty R_\nu i_{\text{vbb}}(T) d\nu,$$

and

$$A_g(T, u) = \frac{\int_0^\infty R_\nu [1 - \exp(-\kappa_\nu(T, u))] d\nu}{\int_0^\infty R_\nu d\nu}. \tag{S4}$$

Thus, the approximate expression of Eq. (6) in the main text is obtained. This approximation was justified by confirming the following relation numerically:

$$\int_0^\infty R_\nu i_{\nu\text{bb}}(T)[1 - \exp(-\kappa_\nu)]d\nu \approx \int_0^\infty R_\nu i_{\nu\text{bb}}(T)d\nu \times \frac{\int_0^\infty R_\nu [1 - \exp(-\kappa_\nu)]d\nu}{\int_0^\infty R_\nu d\nu},$$

and an agreement within 7% accuracy was confirmed.

Here, $I_{\text{Rbb}}(T)$ can be determined by calibration experiments, measuring a uniform blackbody at various temperatures T by the detector with responsivity R_ν . $A_g(T, u)$ is the absorptivity of a uniform CO_2 gas with a temperature T and column number density u . While A_g can also be obtained experimentally, this study uses the A_g values based on HITRAN. We confirmed the consistency between HITRAN and our experimental results. N_2 -diluted CO_2 gases with various column densities of $\zeta = 0\text{--}1.04 \times 10^5$ ppm m (25°C) were encapsulated in a gas cell with CaF_2 windows and a length of $L = 104$ mm, and absorptivity A_g at $T_g = 25^\circ\text{C}$ was determined. The results are shown as open circles in Fig. S1(a). Figure S1(a) also shows A_g values for representative temperatures derived from HITRAN. The experimental results and those by HITRAN at $T_g = 25^\circ\text{C}$ show reasonable agreement. Using HITRAN, it is possible to obtain A_g values at any gas temperature. Figure S1(a) shows that the A_g – u relationship has a small temperature dependence.

Here, the signal difference due to the presence of the gas is

$$\Delta I_R = I_R(u) - I_R(0) \approx A_g(T_g^{\text{eff}}, u) [I_{\text{Rbb}}(T_g^{\text{eff}}) - I_{\text{Rbb}}(T_s)],$$

which is a generalized expression of Eq. (7) in the main text. When $T_s = T_g^{\text{eff}}$, $\Delta I_R = 0$. Thus, we can experimentally determine the effective gas temperature T_g^{eff} as the contrast reversal temperature T_s^{rev} . For a gas with uniform temperature and concentration, $T_s^{\text{rev}} = T_g^{\text{eff}} = T_g$ simply holds. For a nonuniform gas, as discussed in Sec. 2.4 and Fig. 3 in the main text, these temperatures are close to the $1/e$ -width average temperature $T_g^{1/e}$ (Fig. S1(d)): $T_s^{\text{rev}} = T_g^{\text{eff}} \approx T_g^{1/e}$.

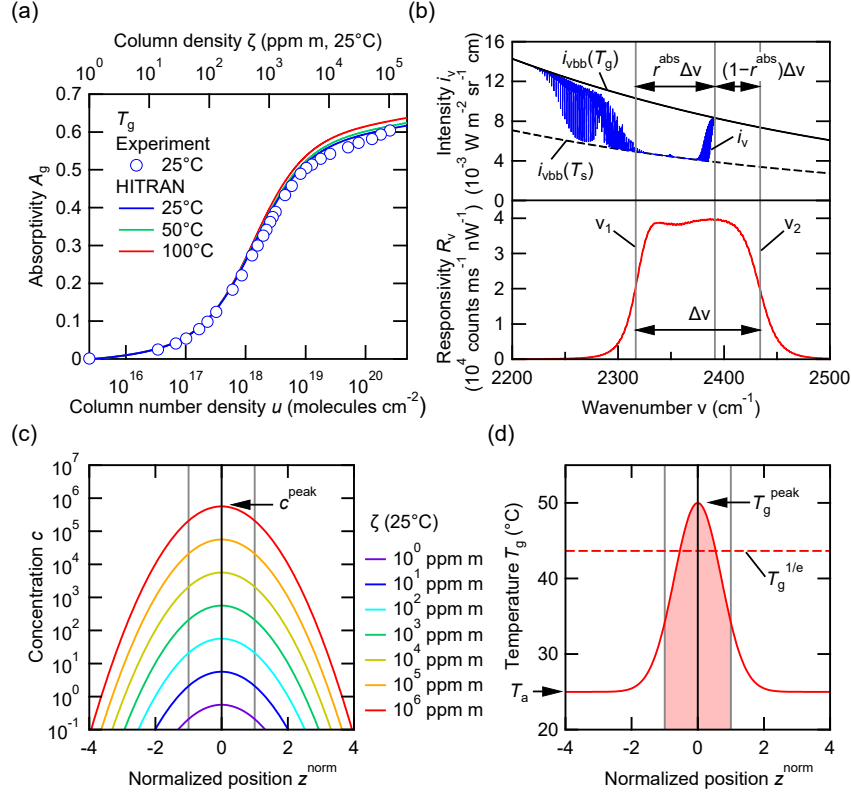


Fig. S1. (a) Relationship between absorptivity A_g and column number density u at several gas temperature T_g values. Experimentally determined A_g (open circles) at $T_g = 25^\circ\text{C}$ and values calculated using Eq. (S4) based on HITRAN at representative T_g values are shown. Upper axis shows corresponding column density ζ for gas at $T_g = 25^\circ\text{C}$ as a reference. (b) Relationship between absorption and transmission bands within the sensitivity band of the camera. Lower panel shows responsivity spectrum R_v with bandwidth $\Delta\nu$ of CO_2 imaging camera used in study, retrieved from Fig. 2(b), main text. Upper panel shows radiation intensity spectrum i_v and blackbody radiation intensities i_{vbb} at $T_g = 50^\circ\text{C}$, light source temperature $T_s = 75^\circ\text{C}$, and $\zeta(50^\circ\text{C}) = 10^4 \text{ ppm m}$, retrieved from Fig. 2(c), main text. The sensitivity bandwidth $\Delta\nu$ can be clearly divided into absorption (width: $r^{\text{abs}}\Delta\nu$) and transmission bands (width: $(1-r^{\text{abs}})\Delta\nu$). (c) Concentration profile of gas assumed in Fig. 3, main text. Gaussian distributions to achieve specific values of column density ζ given in legend are considered, assuming a uniform temperature of 25°C . (d) Temperature profile of gas assumed in Fig. 3, main text. A Gaussian distribution is considered with peak temperature $T_g^{\text{peak}} = 50^\circ\text{C}$, converging to ambient temperature $T_a = 25^\circ\text{C}$ at a sufficiently large distance. In (c) and (d), thickness z^{norm} is normalized by the distance at which Gaussian function decays to $1/e$ of the peak value. In (d), the region within the $1/e$ width is colored red. $T_g^{1/e}$ is the average value in this region, and it is indicated by the horizontal red dashed line.

B. Radiative transfer at a single frequency in nonuniform gas

Figure S2 systematically shows radiative transfer at a single frequency ν for a gas with Gaussian distributions of temperature (Fig. S2(b)) and concentration (Fig. S2(a)). A frequency corresponding to the wavelength of $4.26 \mu\text{m}$ (center of the CO_2 absorption band) is assumed. The relationships between the intensity difference Δi_ν due to the presence of the gas and the light source temperature T_s are very similar to those for the finite bandwidth results in Fig. 3(a)

and (b) in the main text for both the uniform (Fig. S2(c)) and nonuniform distributions (Fig. S2(d)). The relationship between gas concentration (optical thickness κ_v) and contrast reversal temperature T_s^{rev} ($= T_{vg}^{\text{eff}}$) for various peak gas temperature T_g^{peak} values is shown in Fig. S2(e). While absorption is low (i.e., concentration is low), T_s^{rev} remains constant and is close to the $1/e$ -width average temperature $T_g^{1/e}$ shown by the dashed lines at any temperature. The deviation of T_s^{rev} from $T_g^{1/e}$ begins around $\kappa_v \sim 2$, i.e., where absorptivity A_{vg} starts to saturate (Fig. S2(f)). Consequently, the behavior in a finite bandwidth discussed in the main text (Fig. 3) is essentially identical to the monochromatic case. The fact that T_s^{rev} is close to $T_g^{1/e}$ suggests the universal importance of the $1/e$ -width average value in systems with a temperature distribution.

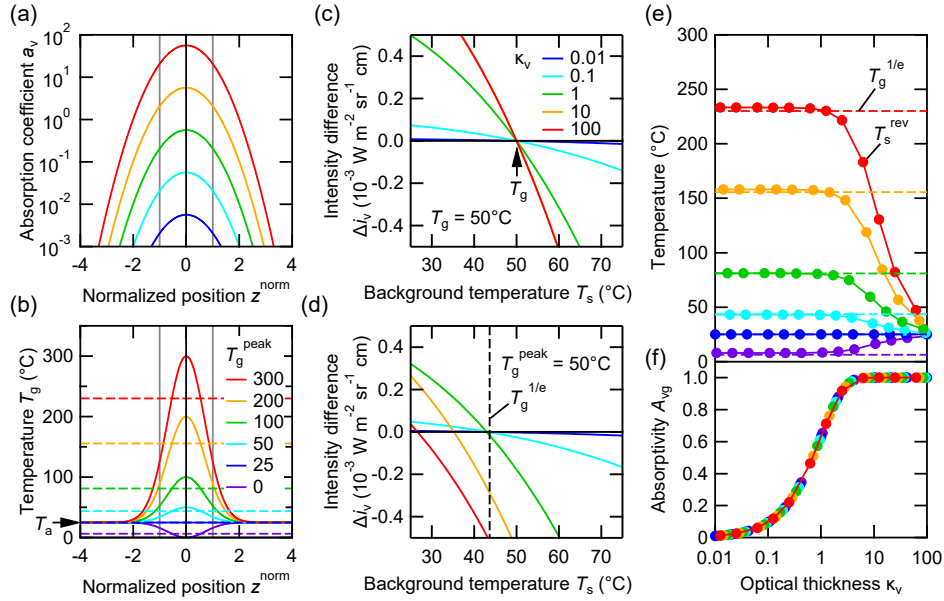


Fig. S2. (a) Gas concentration profiles with Gaussian distributions having various optical thicknesses κ_v (legend in (c)). (b) Gas temperature profiles with Gaussian distributions having various peak temperatures T_g^{peak} at ambient temperature $T_a = 25^\circ\text{C}$. (c) Contrast reversal at a certain frequency ν for uniform gases with gas temperature $T_g = 50^\circ\text{C}$ and various κ_v , during sweeping of light source (background) temperature T_s . (d) Contrast reversal at a certain ν for nonuniform gases with Gaussian distributions of temperature ($T_g^{\text{peak}} = 50^\circ\text{C}$) and concentrations (κ_v in (c)), in T_s sweeping. (e) Relationship between contrast reversal temperature T_s^{rev} and concentration (κ_v) at a certain ν for gases with various T_g^{peak} (legend in (b)) with Gaussian distributions. Dashed lines show $1/e$ -width average temperature $T_g^{1/e}$. (f) Relationship between absorptivity A_{vg} and κ_v for gases with various T_g^{peak} in (e).

C. Correction considering the influence of background layer

C.1 Influence of optical properties of light source

A correction that considers the influence of the background layer is discussed here based on Fig. S3. The space is divided into three layers: the background layer between the light source

surface and the gas layer, the gas layer itself, and the foreground layer between the gas layer and the camera [2–5]. The intensity signal at the end of each region, giving consideration to the responsivity spectrum of the camera, is defined as I_0 , I_1 , I_2 , and I_3 at the emission surface of the light source, the end of the background layer, the end of the gas layer, and the entrance of the camera lens, respectively. Moreover, the light source may have an internal structure. For example, the light source B and C used in this study had an anti-reflection-coated Si window for vacuum encapsulation. The light source temperature T_s discussed so far should be regarded as the equivalent temperature at the emission surface. The true emissivity and temperature of the internal radiating surface of the light source are ϵ_s and T_s^{org} , and the window transmissivity is τ_s . The emission signal from the surface of a light source without a window (like the light source A in this study) is $I_0 = \epsilon_s I_{\text{Rbb}}(T_s^{\text{org}})$. For a light source with a window, $I_0 = \tau_s \epsilon_s I_{\text{Rbb}}(T_s^{\text{org}}) + (1 - \tau_s) \epsilon_{\text{env}} I_{\text{Rbb}}(T_a)$. The second term shows the component where the environmental radiation is reflected by the window surface and directed toward the camera. ϵ_{env} and T_a are the emissivity (assumed to be ~ 1) and temperature of the surrounding environment. So far, such a value of I_0 has been regarded as $I_{\text{Rbb}}(T_s)$.

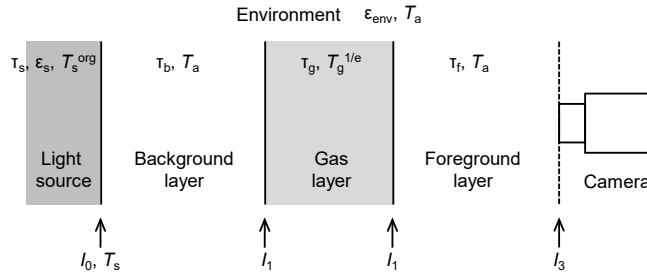


Fig. S3. Schematic diagram of three-layer model for considering atmospheric CO_2 absorption/emission and optical system characteristics. Transmissivity, emissivity, and temperature of each part are shown.

C.2 Influence of atmospheric CO_2 in background space

Consider the transmissivities τ_b and τ_f for the background and foreground layers, respectively, and suppose that their temperatures are equal to the ambient temperature T_a . The transmissivity of the gas τ_g is also used ($A_g = 1 - \tau_g$). The intensity signals at the end of each region are given as

$$I_1 = \tau_b I_{\text{Rbb}}(T_s) + (1 - \tau_b) I_{\text{Rbb}}(T_a),$$

$$I_2 = \tau_g [\tau_b I_{\text{Rbb}}(T_s) + (1 - \tau_b) I_{\text{Rbb}}(T_a)] + (1 - \tau_g) I_{\text{Rbb}}(T_g^{1/e}),$$

and

$$I_3 = \tau_f \left\{ \tau_g [\tau_b I_{\text{Rbb}}(T_s) + (1 - \tau_b) I_{\text{Rbb}}(T_a)] + (1 - \tau_g) I_{\text{Rbb}}(T_g^{1/e}) \right\} + (1 - \tau_f) I_{\text{Rbb}}(T_a).$$

In the absence of gas,

$$I_3^{\text{no gas}} = \tau_f [\tau_b I_{\text{Rbb}}(T_s) + (1 - \tau_b) I_{\text{Rbb}}(T_a)] + (1 - \tau_f) I_{\text{Rbb}}(T_a).$$

The signal difference due to the presence of the gas is

$$\Delta I_3 = \tau_f A_g \left[I_{\text{Rbb}}(T_g^{1/e}) - \tau_b I_{\text{Rbb}}(T_s) - (1 - \tau_b) I_{\text{Rbb}}(T_a) \right]. \quad (\text{S5})$$

The property of the foreground τ_f has no effect on the contrast reversal temperature at $\Delta I_3 = 0$.

C.3 Influence of transmission/absorption regions within imaging bandwidth

For the CO₂ camera used in this study, another factor must be considered. As shown in Fig. 2(a) and (b) in the main text, there is a designed mismatch between the responsivity band of the camera and the absorption band of the CO₂ gas. Therefore, even if the column density of the gas is sufficiently high and the gas becomes totally opaque, a certain amount of light still enters the camera through the transmission band. As a result, gas absorptivity A_g does not reach 1. Since the signal due to the transmission band does not change regardless of the presence or absence of the gas, it is canceled when obtaining the difference between I_3 and $I_3^{\text{no gas}}$ and does not contribute to ΔI_3 . Therefore, intensity signal I_3 must be further divided into absorption and transmission band components, denoted with superscripts *abs* and *tra*, respectively. The absorption and transmission bandwidths within the total camera bandwidth $\Delta\nu$ are written as $r^{\text{abs}}\Delta\nu$ and $(1 - r^{\text{abs}})\Delta\nu$, respectively (Fig. S1(b)). At $T_g=25^\circ\text{C}$, based on A_g for $\zeta = 10^6$ ppm m in Fig. S1(a), r^{abs} is taken as 0.636. Within I_3 , the intensity signal of the absorption and transmission bands are $r^{\text{abs}}I_3$ and $(1 - r^{\text{abs}})I_3$, respectively. Here, it is assumed that the blackbody radiation intensity spectrum has a flat ν dependence (Fig. S1(b), upper). For the absorptivity A and transmissivity τ ($A = 1 - \tau$) for the total bandwidth $\Delta\nu$, the absorptivity A^{abs} and transmissivity τ^{abs} within the absorption band are expressed as $A^{\text{abs}} = A/r^{\text{abs}}$ and $\tau^{\text{abs}} = 1 - A/r^{\text{abs}}$, respectively.

I_3 can be separated into each band as follows:

$$\begin{aligned} I_3^{\text{abs}} &= \tau_f^{\text{abs}} \\ &\left\{ \tau_g^{\text{abs}} [\tau_b^{\text{abs}} r^{\text{abs}} I_{\text{Rbb}}(T_s) + (1 - \tau_b^{\text{abs}}) r^{\text{abs}} I_{\text{Rbb}}(T_a)] + (1 - \tau_g^{\text{abs}}) r^{\text{abs}} I_{\text{Rbb}}(T_g^{1/e}) \right\} + \\ &(1 - \tau_f^{\text{abs}}) r^{\text{abs}} I_{\text{Rbb}}(T_a), \\ I_3^{\text{tra}} &= (1 - r^{\text{abs}}) I_{\text{Rbb}}(T_s). \end{aligned}$$

In the absence of gas,

$$\begin{aligned} I_3^{\text{abs, no gas}} &= \tau_f^{\text{abs}} [\tau_b^{\text{abs}} r^{\text{abs}} I_{\text{Rbb}}(T_s) + (1 - \tau_b^{\text{abs}}) r^{\text{abs}} I_{\text{Rbb}}(T_a)] + (1 - \tau_f^{\text{abs}}) r^{\text{abs}} I_{\text{Rbb}}(T_a), \\ I_3^{\text{tra, no gas}} &= (1 - r^{\text{abs}}) I_{\text{Rbb}}(T_s) = I_3^{\text{tra}}. \end{aligned}$$

Therefore, the signal difference due to the presence of the gas is

$$\begin{aligned} \Delta I_3 &= (I_3^{\text{abs}} + I_3^{\text{tra}}) - (I_3^{\text{abs, no gas}} + I_3^{\text{tra, no gas}}) \\ &= \tau_f^{\text{abs}} A_g^{\text{abs}} r^{\text{abs}} \left[I_{\text{Rbb}}(T_g^{1/e}) - \tau_b^{\text{abs}} I_{\text{Rbb}}(T_s) - (1 - \tau_b^{\text{abs}}) I_{\text{Rbb}}(T_a) \right] \\ &= \tau_f^{\text{abs}} A_g \left[I_{\text{Rbb}}(T_g^{1/e}) - \tau_b^{\text{abs}} I_{\text{Rbb}}(T_s) - (1 - \tau_b^{\text{abs}}) I_{\text{Rbb}}(T_a) \right]. \end{aligned} \quad (\text{S6})$$

In comparing this Eq. (S6) with Eq. (S5), even after correction for the transmission and absorption bands, A_g remains the same (absorptivity defined for total bandwidth $\Delta\nu$). However, τ_f and τ_b must be replaced by τ_f^{abs} and τ_b^{abs} . By defining

$$I_{\text{Rbb}}(T_s^{\text{eff}}) = \tau_b^{\text{abs}} I_{\text{Rbb}}(T_s) + (1 - \tau_b^{\text{abs}}) I_{\text{Rbb}}(T_a),$$

as in Eq. (8) in the main text, Eq. (7) is modified as

$$\Delta I_3 = \tau_f^{\text{abs}} A_g \left[I_{\text{Rbb}}(T_g^{1/e}) - I_{\text{Rbb}}(T_s^{\text{eff}}) \right].$$

When $\Delta I_3 = 0$, we can determine the $1/e$ -width average temperature of the gas as $T_g^{1/e} = T_s^{\text{eff}}$.

In summary, if the effective transmission source temperature T_s^{eff} is considered according to Eq. (8) in the main text to account for the effect of background CO₂, the conclusion stands that the contrast reversal temperature T_s^{rev} can be regarded as the gas temperature $T_g^{1/e}$.

In this study, the $I_{\text{Rbb}}(T)$ needed for Eq. (8) was measured at various temperatures for the system, including the camera lens. Therefore, I_{R} in the main text is equivalent to I_3 in this section, which can thus be read as I_{R} .

The transmissivity of the background layer in the absorption band $\tau_{\text{b}}^{\text{abs}}$ can be determined from absorptivity A_{b} , corresponding to column density ζ in the background layer (Fig. S1(a)) and then by applying $\tau_{\text{b}}^{\text{abs}} = 1 - A_{\text{b}}/r^{\text{abs}}$.

The contrast reversal method is essentially a null method: The measurement error is determined by the accuracy of the light source temperature. However, only in the case of CO_2 measurement, background correction in Eq. (8) (main text) becomes necessary due to the substantial amount of CO_2 contained in the atmosphere. Therefore, temperature accuracy could be affected by the estimation of $\tau_{\text{b}}^{\text{abs}}$ discussed here. The correction by Eq. (8) in this work ranged from 0.1°C (at $T_{\text{g}}^{1/e} \sim 25^\circ\text{C}$) to 8°C (at $T_{\text{g}}^{1/e} \sim 100^\circ\text{C}$). Temperature error due to improper estimation of $\tau_{\text{b}}^{\text{abs}}$ would be only a fraction of these values (a few $^\circ\text{C}$ at most).

D. Experimental methods

D.1 Details of CO_2 imaging camera

The FLIR A6796 is an InSb camera equipped with a bandpass filter having the transmission profile shown in Fig. 2(b), main text. Although both the image sensor and filter require cooling to 80 K, the camera can be operated by battery power. The image resolution is 640×512 pixels, and the maximum frame rate is 480 fps. A variety of FLIR lenses (F2.5) can be mounted, and various data analyses are possible. The intensity resolution is 14-bit, and signals exceeding 10^5 counts can be obtained without saturation. On the other hand, signal differences as small as $\lesssim 10$ counts can be distinguished. Therefore, the dynamic range of intensity is 10^3 or higher. The signal can be adjusted to fit this range by selecting the exposure time t_{exp} . The noise equivalent differential temperature (NEDT), an important metric for infrared cameras, was measured at 28 mK at 25°C . This value is inferior to that of the original InSb camera (18 mK), but it is reasonable considering the reduction in signal due to the bandwidth limitation.

Although a CO_2 imaging camera, the GF343 from FLIR [6,7], is commercially available, it has limitations in pixel count, available settings, and lens choices. Therefore, we asked FLIR to provide a custom-made A6796 that combines a scientific-grade InSb camera with a built-in cooled filter for CO_2 [8].

D.2 Instruments used in this work

Two types of thermocouples, with 13- μm and 50- μm diameters, were used (Anbe SMT, KFT-13-200-100 and KFT-50-200-100, respectively). Thermocouple temperatures were recorded with a data logger (Hioki, LR8431). The following CO_2 sensors were used depending on the target: Hodaka, HT-1300Z type D and Kane, KANE455 for concentration and temperature of hot and high-density CO_2 , Vaisala, GMP252/MI70 for environmental CO_2 concentration, and a capnometer, Medtronic, Capnostream35 for CO_2 concentration in human breath. We also used a spirometer, Chest, HI-801 for emission rate of human breath and a radiation thermometer, Tanita, BT-54X for body temperature. The blackbody radiation surface temperature was calibrated with a calibrated temperature sensor (Lake Shore, DT-670-CU-HT-1.4H). The emissivity (absorptivity) of the blackbody paint and the transmissivity of the silicon window were measured using FTIR (JASCO, FT/IR-6200) equipped with a microscope unit, IRT-5000.

E. Temperature measurement of intermittently emitted gas

The intensity in the CO₂ image of intermittently ejected gas is discussed in accordance with Sec. 2.3 in the main text. For simplicity, it is assumed that gas with constant CO₂ concentration and temperature is emitted as rectangular pulses. As shown in the bottom and middle panels of Fig. S4(a), the absorptivity changes between 0 and its maximum value, and the temperature changes between room temperature T_a and its maximum. Under these conditions, according to Eqs. (6) and (7) in the main text, the signal difference ΔI_R varies in a rectangular manner between 0 and a certain peak value, as shown in the top panel. When the gas is not being emitted, the concentration and thus the absorptivity are 0, so ΔI_R becomes 0. The height of nonzero ΔI_R , as shown in Eq. (7) (main text), is given by the difference between the blackbody radiation functions of the gas temperature T_g and the light source temperature T_s . As shown in Fig. 9(d), main text, when T_s (T_s^{eff}) is varied, the height of the rectangular signal changes and the sign of ΔI_R reverses at a certain T_s^{eff} . This T_s^{eff} is equal to the gas temperature T_g . Therefore, by selectively observing the nonzero ΔI_R , the same discussion as the contrast reversal method for continuous gas emissions applies.

Next, the exhaust gas of the internal combustion engine in Sec. 5.2, main text, is considered. Each cylinder of a diesel engine completes one cycle in two rotations (720 degrees). Assuming that the exhaust valve is open during the final 180 degrees of the second rotation, the timing of gas emission during one cycle of a three-cylinder engine is shown in Fig. S4(b). The image exposure cycle at 30 fps is also shown. The exhaust frequency (22.5 Hz) for 900 rpm rotation and this frame rate have similar values. The exposure time is sufficiently shorter than the exhaust cycle, so each frame captures either the emission or halt phase. It is probabilistically determined whether an emission or halt scene is captured; in the case of Fig. S4(b), about 75% of frames (33.3 ms/44.4 ms) are expected to capture the emission phase and 25% (11.1 ms/44.4 ms) the halt phase.

Individual frames are displayed in Fig. S5. Of the 30 frames captured in one second, 7 did not capture any gas (23%). Two were transitional. The discussion given in Fig. S4(b) closely corresponds to the actual situation.

Figure S4(c) is a schematic representation of exhalation, which produces slow intermittent emissions. In each emission and halt period, a number of images are recorded; consequently, a clear selection of only those images during exhaust is possible.

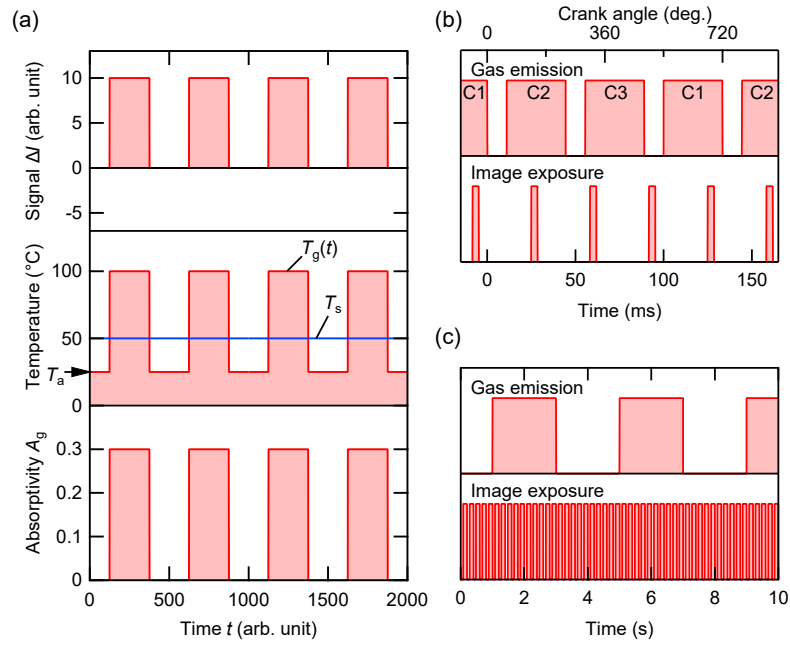


Fig. S4. Fundamental discussion on temperature measurement of intermittently emitted gas. (a) Changes in gas absorptivity A_g (corresponding to concentration) and temperature T_g are presented in bottom and middle panels, respectively. Absorptivity is assumed to change between 0 and its maximum value, and temperature between ambient temperature T_a and its maximum value, both in a rectangular shape. Light source (background) temperature T_s is shown as a blue line in middle panel. Corresponding signal difference ΔI_R is shown in top panel. (b) Time chart showing engine gas emission and image acquisition. Cylinders C1, C2, and C3 emit gas sequentially at equal intervals. Images are acquired at a similar frequency. (c) Time chart for exhaled breath emission and image acquisition. Breathing is slow relative to image acquisition.

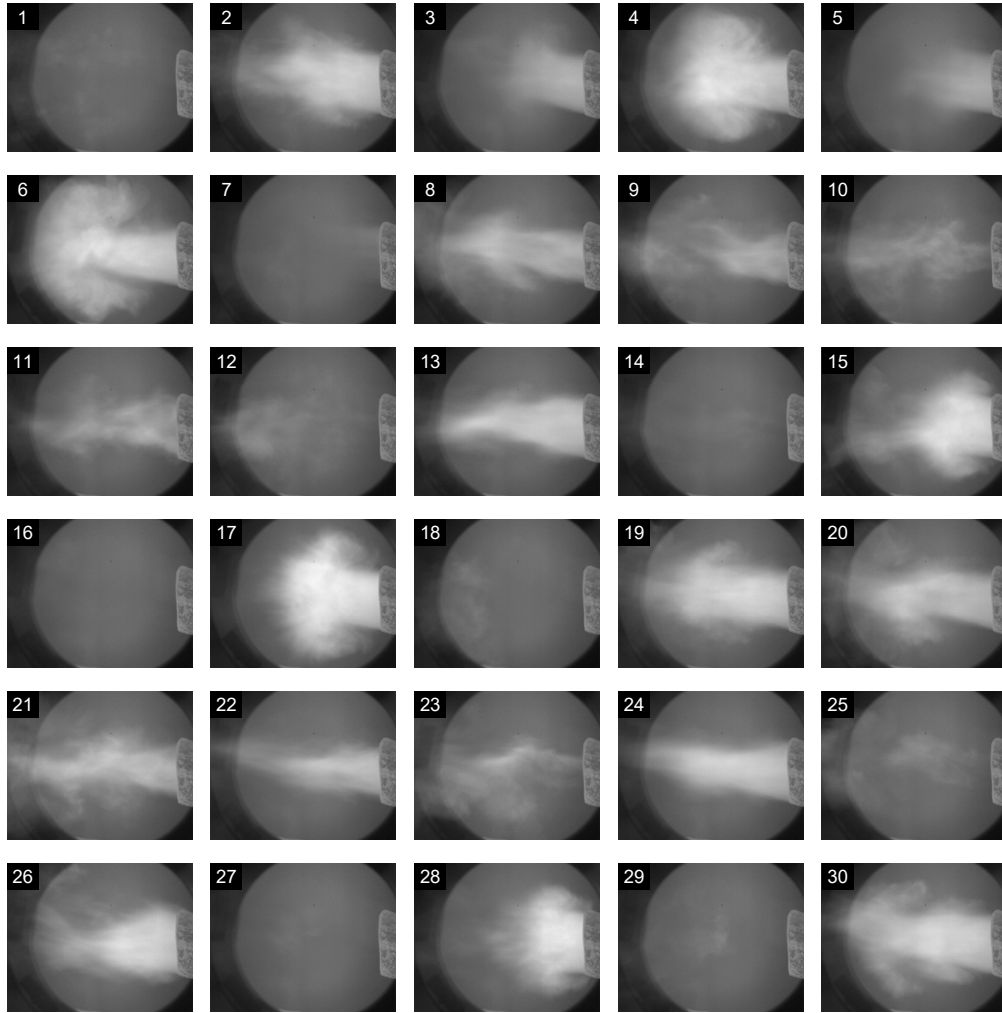


Fig. S5. Consecutive images (frames 1–30) of diesel engine exhaust at effective light source temperature $T_s^{\text{eff}} = 31.8^\circ\text{C}$ as discussed in Sec. 5.2, main text. Gas is nearly absent in seven frames 1, 7, 14, 16, 18, 27, and 29. Thin residual gas is seen in two frames 12 and 25. Mushroom-shaped emission patterns in frames 2, 4, 15, 17, 28, and 30 suggest origin of temperature peak at 30 mm from exhaust outlet.

F. Detailed discussion related to human exhalation

The temperatures of exhaled breath measured at a position 10 mm from the mouth or nose using a 50- μm thermocouple are shown in Fig. S6. The measurement results for mouth exhalation (Fig. S6(a)) were stably obtained. In contrast, the temperature of the nasal exhalation (Fig. S6(b)) fluctuated greatly. We considered the average of the top 20% data points (shown in red, measured from the valleys defining individual peaks) as the exhalation temperature. The average was 31.9°C for the mouth and 31.0°C for the nose. The result that exhalation from the mouth was 0.9°C higher than that from the nose was consistent for both imaging and measurement by thermocouple.

Careful observation of the signal difference ΔI_R of exhalation from the mouth and nose revealed a number of interesting findings, as shown in Figs. S7 and S8. Breathing starts between frames 1 and 10, and frames 10–44 show monotonic exhalation. Exhaled breath from both the

mouth and nose appear bright in Fig. S8. However, at frame 45, nasal emission stops once (A, Fig. S7), although the mouth continues exhalation. In the next moment (frame 46), nasal emission resumes and exhibits a large, bright exhaust from the nose at frame 47 (B, Fig. S8). Then, at frame 49, both nasal and oral emissions stop (C), as indicated by the vertical line in Fig. S7. Nevertheless, exhalation from both the nose and mouth resumes at frame 50, reaching another peak in frame 53 (D, Fig. S7). After this, exhalation weakens and emission ends. Previously exhaled breath remains in the nasal area as a dark cloud (Fig. S8). This corresponds to the invalid region of the nose shown in gray in the upper panel of Fig. S7.

Sudden stops and resumptions of breath occurred within a single frame, i.e., within only 40 ms. Such quick changes within a single frame were frequently observed. Although medical discussion is beyond the scope of this paper, it is important to note that these observed phenomena, which can only be captured by this method, merit further study.

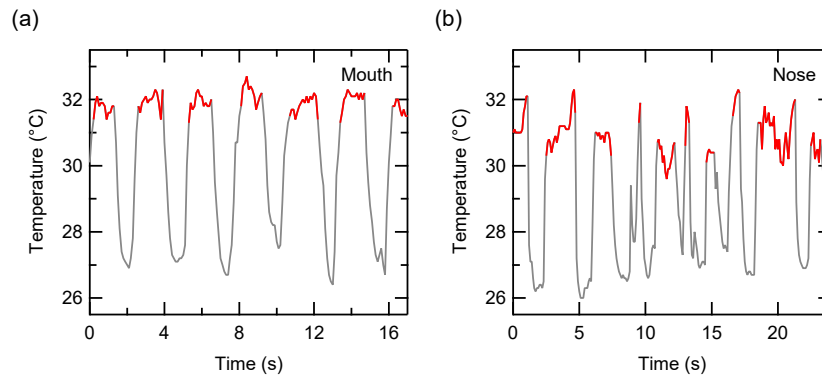


Fig. S6. Results of measuring breath temperature by thermocouple: (a) mouth and (b) nose, both at a distance of 10 mm.

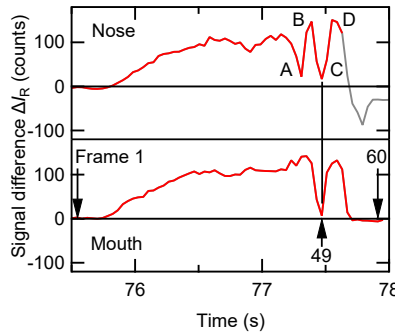


Fig. S7. Temporal variation in mouth and nose signal difference ΔI_R for breath B21. Representative frame numbers corresponding to Fig. S8 are denoted. For the nose after 77.6 s, values are invalid due to overlapping with previously emitted, cooled breath (gray). Other clear features, A, B, C, and D, represent meaningful findings.

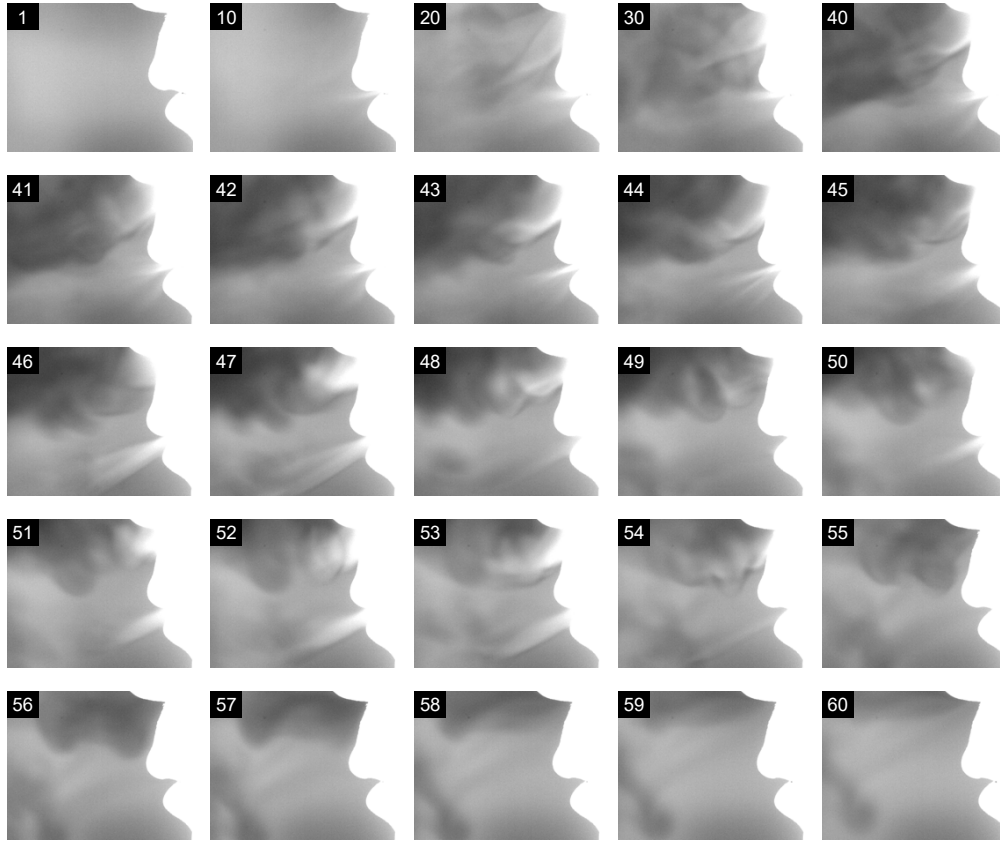


Fig. S8. Representative images during breath B21 at effective light source temperature $T_s^{\text{eff}} = 30.9^\circ\text{C}$. Correspondence between important features in Fig. S7 and frame numbers are as follows: A: frame 45, B: 47, C: 49, and D: 53.

References

1. I. E. Gordon, L. S. Rothman, R. J. Hargreaves, *et al.*, “The HITRAN2020 molecular spectroscopic database,” *J. Quant. Spectrosc. Radiat. Transfer* **277**, 107949 (2022).
2. M. L. Polak, J. L. Hall, and K. C. Herr, “Passive Fourier-transform infrared spectroscopy of chemical plumes: an algorithm for quantitative interpretation and real-time background removal,” *Appl. Opt.* **34**(24), 5406–5412 (1995).
3. A. Ben-David and C. E. Davidson, “Probability theory for 3-layer remote sensing radiative transfer model: univariate case,” *Opt. Express* **20**(9), 10004–10033 (2012).
4. M. A. Rodríguez-Conejo and J. Meléndez, “Hyperspectral quantitative imaging of gas sources in the mid-infrared,” *Appl. Opt.* **54**(2), 141–149 (2015).
5. N. Hagen, “Survey of autonomous gas leak detection and quantification with snapshot infrared spectral imaging,” *J. Opt.* **22**(10), 103001 (2020).
6. B. Murphy, R. Cahill, C. McCaul, *et al.*, “Optical gas imaging of carbon dioxide at tracheal extubation: a novel technique for visualising exhaled breath,” *Br. J. Anaesth.* **126**(2), e77–e78 (2021).
7. Y. Peng and M. Yao, “Quantitatively visualizing airborne disease transmission risks of different exhalation activities through CO_2 imaging,” *Environ. Sci. Technol.* **57**(17), 6865–6875 (2023).
8. M. Morioka, Y. Takamura, H. T. Miyazaki, *et al.*, “Relationship between surgical field contamination by patient’s exhaled air and the state of the drapes during eye surgery,” *Sci. Rep.* **13**, 5713 (2023).